Control of the separated flow around an airfoil using a wavy leading edge inspired by humpback whale flippers

Julien Favier, Alfredo Pinelli, Ugo Piomelli

Control of the separated flow around an airfoil using a wavy leading edge inspired by humpback whale flippers

Julien Favier [a], Alfredo Pinelli [a], Ugo Piomelli [b]

[a] *CIEMAT, Unidad de Modelización y Simulación Numérica, 28040 Madrid, Spain*

[b] *Dept. of Mechanical and Materials Engineering, Queen's University, Kingston (Ontario) K7L 3N6, Canada*

Received *****; accepted after revision +++++

Presented by

Abstract

The influence of spanwise geometrical undulations of the leading edge of an infinite wing is investigated numerically at low Reynolds number, in the context of passive separation control and focussing on the physical mechanisms involved. Inspired by the tubercles of the humpback whale flippers, the wavy leading edge is modeled using a spanwise sinusoidal function whose amplitude and wavelength constitute the parameters of control. A direct numerical simulation is performed on a NACA0020 wing profile with massive separation on the suction side ($\alpha = 20^o$), with and without the presence of the leading edge waviness. The complex solid boundaries obtained by varying the sinusoidal shape of the leading edge are modeled using an immersed boundary method (IBM) recently developed by the authors [Pinelli et al. *J. Comput. Phys.* 229 (2010) 9073–9091]. A particular set of wave parameters is found to change drastically the topology of the separated zone, which becomes dominated by streamwise vortices generated from the sides of the leading edge bumps. A physical analysis is carried out to explain the mechanism leading to the generation of these coherent vortical structures. The role they play in the control of boundary layer separation is also investigated, in the context of the modifications of the hydrodynamic performances which have been put forward in the literature in the last decade. *To cite this article: J. Favier, A. Pinelli, U. Piomelli, C. R. Mecanique ??? (2011).*

Résumé

Contrôle du décollement autour d'un profil d'aile présentant un bord d'attaque ondulé inspiré des ailerons de la baleine à bosse. L'influence d'ondulations géométriques le long du bord d'attaque d'un profil d'aile est étudiée numériquement à faible nombre de Reynolds, dans une optique de contrôle passif du décollement et en se focalisant sur les mécanismes physiques mis en jeu. Inspiré des tubercules présents sur les ailerons des baleines à bosse, ce bord d'attaque ondulé est modelisé par une sinusoïde le long de l'envergure, dont la longueur d'onde et l'amplitude constituent les paramètres de contrôle. Une simulation numérique directe est effectuée sur un profil NACA0020 dans une configuration d'écoulement massivement décoll'e ($\alpha = 20^o$), avec et sans ondulation de bord d'attaque. Les frontières solides complexes engendrées par la variation des paramètres de l'ondulation géométrique sont traitées par la méthode des frontières immergées (IBM). Les noyaux des opérateurs d'interpolation/diffusion sont construits en utilisant la méthode RKPM [12]. Une étude paramétrique permet d'extraire un jeu de paramètres d'ondulation qui amène à une modification significative de la topologie de l'écoulement décollé, qui se retrouve dominé par des tourbillons orientés vers l'aval et générés sur les cotés des protubérances de bord

d'attaque. Une analyse physique est menée pour expliquer le mécanisme de formation de ces structures cohérentes tourbillonnaires. Le rôle qu'elles jouent dans le contrôle du décollement de couche limite est étudié également, sous l'éclairage des modifications de performances hydrodynamiques présentées dans la littérature au cours de la dernière décennie. *Pour citer cet article : J. Favier, A. Pinelli, U. Piomelli, C. R. Mecanique ? ? ? (2011).*

Key words: Flow control ; Biomimetics ; Immersed Boundary ; humpback whale flippers

Mots-clés : Contrôle d'écoulements ; biomimétisme ; Méthode des frontières immergées ; ailerons de baleines à bosse

1. Introduction

The humpback whale, *Megaptera novæangliæ*, is one of the most massive animals living in the oceans; at the same time, this whale is well known for astonishing maneuvering capabilities. One of the features of this mammal that affect its hydrodynamic performance is its very specific surface geometry, made of protuberances, especially on the leading edges of the pectoral flippers, called tubercles (Figure 1), which inspired the present work. Tubercles are the result of a long process of multiple-task natural optimization: they may have for instance thermo-regulation purposes in addition to their hydrodynamical role [1]. Thus, the structural and shape parameters of the flipper may be suboptimal, as far as only hydrodynamics are concerned. Nonetheless, there is some interest in understanding the hydrodynamical features of tubercles, to adapt them to technological applications, within the renewed interest that biomimetics has recently received.

The potential benefits of tubercles on the aerodynamic performances of a wing airfoil were suggested by Bushnell & Moore [2] and later, from a more morphological point of view, by Fish & Battle [3], who showed that the geometrical properties of the tubercles can influence the aerodynamical performances of a wing. It was believed since the beginning that the tubercles would have an influence on stall, delaying the angle of attack at which lift decreases, and also reducing the form drag at high angles of attack.

Several studies were performed over the last two decades to assess the influence of the tubercles, both experimentally and numerically. The first numerical study was performed by Watts & Fish, using a numerical 3D panel method [4]; they found a slight increase of lift coefficient (4.8%) and a 11% reduction of drag for a pre-stall angle of attack. The wind tunnel experiments of Miklosovic et al. [5] exhibited drastic enhancements of lift for a post-stall angle of attack, also showing a delay of 40% of the stall angle. Both studies were performed at Reynolds numbers of the order of $Re = 10^5$ (lower than those observed in nature). More recent experiments confirmed these findings as far as the action of bumps on stall at similar Reynolds numbers is concerned [1,6]. In 2003, Patterson et al. [7] solved the Unsteady

Email address: Julien.favier@ciemat.es (Julien Favier).

Figure 1. The Humpback whale jumping out of water. The pectoral flipper clearly exhibits tubercles on the leading edge.

Reynolds-Averaged Navier-Stokes (URANS) equations, and showed that the tubercles can modify the shape on the recirculating zone and improve global performances. A simpler approach was explored by Van Nierop et al. [8], who used the Kutta condition to estimate the circulation Γ in a potential flow model. Globally the numerical and experimental studies converge towards similar conclusions, but, as pointed out by in Ref. [8], the underlying physical mechanisms and the associated fluid flow features still remain unclear, although there are speculations about the action of the bumps as vortex generators [9], which create vortical structures similar from those emitted at the tip of a delta wing [1]. The experimental study by Stanway [1] also investigated, by means of PIV, the effect of the tubercles on the dynamic stall (as opposed to the static stall studied before) by flapping the wing. Different behaviours were observed in the static and dynamic cases, and the efficiency parameters for a fixed wing are not necessarily the same as those for a flapping one.

In this work we present a three-dimensional Direct Numerical Simulation of Navier-Stokes equations, focussing on the effect of the protuberances on the topology of the flow at low Reynolds number. Our goal is to obtain an insight of the underlying physical mechanism responsible of the hydrodynamic performance enhancements in the absence of transitional effects, or a broadband perturbation spectrum; the Reynolds number, based on the free stream velocity and the chord length, is, therefore, chosen to be $Re = 800$; this value is lower than that associated with transition to turbulence, but at this Reynolds number, the wake experiences three-dimensional effects issued from the first spanwise instabilities rising before transition to turbulence [10]. Although this value is much lower than the one observed in nature, it may allow us to obtain a first picture of the physical mechanism responsible of the performances enhancements. As the morphological parameters of the humpback whale flippers are similar to those of a wing section [3] with a thickness of approximately 20% of the chord length, we will perform our investigation on a static NACA0020 wing airfoil, whose chord can vary along the span to model the protuberances. The angle of attack is fixed to $\alpha = 20^o$, a configuration corresponding to a massive boundary layer separation.

In the following, we will first describe briefly the numerical method that has been used. We will then present some results, including quantitative measures of the lift and drag modifications, as well as instantaneous flow visualizations. On the basis of the results obtained, we will propose a conceptual mechanism to explain the different flow topologies encountered in the fluid flow in the presence of different configurations of leading edge undulations. We will finally draw concluding remarks and recommendations for future works.

2. Problem formulation

2.1. *Numerical Method*

In this work we use an Immersed Boundary Method (IBM) to enforce the presence and effects of the body in the fluid flow. With this approach, the grid is not required to conform to the body geometry, and the solid wall boundary conditions are satisfied on the body surface by using appropriate boundary forces [11,12]. This allows to simulate a range of complex geometries on a cartesian grid, using fast and accurate solvers that conserve discretely the mechanical energy of the flow, and are, therefore, suitable to the simulation of transitional cases.

We use a three-dimensional incompressible Navier-Stokes solver to model the fluid flow. The equations are discretized on a staggered grid system [13]. Both convective and diffusive fluxes are approximated by second-order centered differences. The fractional time-step method is used for the time-advancement [14,15], in the form of a second-order semi-implicit pressure correction procedure [16]. The alternating direction implicit method (ADI) is used for the temporal discretization of the diffusive terms,

allowing to transform three-dimensional problem into three one-dimensional ones by an operator-splitting technique, while retaining the formal order of the scheme. The solution of the three-dimensional pressure Poisson equation, needed to carry out the correction step, is also reduced into a series of two-dimensional Helmoltz equations by performing a Fourier transform in the spanwise direction, z, and solving two-dimensional problems for each wavenumber using a fast block-tridiagonal solver. The code parallelization relies upon the Message-Passing Interface (MPI) library and the domain-decomposition technique.

The numerical strategy used to impose the desired zero velocity boundary condition at the solid surface (which is a solid and rigid wing) is the following: we first obtain the predicted velocity, $\mathbf{u}^*$, explicitly, without the presence of the embedded boundary:

$$\mathbf{u}^* = \mathbf{u}^n - \Delta t \left[\mathcal{N}_l(\mathbf{u}^n, \mathbf{u}^{n-1}) - \mathcal{G}\phi^{n-1} + \frac{1}{Re}\mathcal{L}(\mathbf{u}^n) \right], \tag{1}$$

where $\mathbf{u}^n$ is the divergence-free velocity field at time-step n, Δt is the time step, $\mathcal{N}_l$ is the discrete non-linear operator, $\mathcal{G}$ and $\mathcal{D}$ are, respectively, the discrete gradient and divergence operators, $\mathcal{L}$ is the discrete Laplacian, ϕ is a projection variable (related to the pressure field). The operators include coefficients that are specific to the time scheme used in this study, a three-steps low-storage Runge Kutta.

Next, the presence of the solid geometry is imposed by using the IBM, via a process of interpolation and spreading [17]: $\mathbf{u}^*$ is interpolated onto the embedded geometry of the obstacle, Γ, which is discretized through a number of Lagrangian marker points with coordinates $\mathbf{X}_k$:

$$\mathbf{U}^*(\mathbf{X}_k, t^n) = \mathcal{I}(\mathbf{u}^*) \tag{2}$$

At this stage, knowing the velocity $\mathbf{U}^*(\mathbf{X}_k, t^n)$ at location of the Lagrangian markers, we are able to determine a distribution of singular forces that restore the desired zero velocity values $\mathbf{U}^\Gamma(\mathbf{X}_k, t^n)$ on Γ:

$$\mathbf{F}^*(\mathbf{X}_k, t^n) = \frac{\mathbf{U}^\Gamma(\mathbf{X}_k, t^n) - \mathbf{U}^*(\mathbf{X}_k, t^n)}{\Delta t}. \tag{3}$$

The singular surface force field given over Γ is then transformed by a spreading operator $\mathcal{C}$ into a volume force-field defined on the Cartesian mesh points $\mathbf{x}_{i,j,k}$ surrounding Γ:

$$\mathbf{f}^*(\mathbf{x}_{i,j,k}, t^n) = \mathcal{C}\left[\mathbf{F}^*(\mathbf{X}_k, t^n)\right]. \tag{4}$$

The predicted velocity is then re-calculated, using an implicit scheme for the viscous operator, adding the forces that accounts for the presence of the solid body:

$$\frac{\mathbf{u}^* - \mathbf{u}^n}{\Delta t} = -\mathcal{N}_l(\mathbf{u}^n, \mathbf{u}^{n-1}) - \mathcal{G}\phi^{n-1} + \frac{1}{Re}\mathcal{L}(\mathbf{u}^*, \mathbf{u}^n) + \mathbf{f}^* \tag{5}$$

Finally, the algorithm completes the time step with the usual solution of the pressure Poisson equation and the consequent projection step:

$$\mathcal{L}\phi = \frac{1}{\Delta t}\mathcal{D}\mathbf{u}^* \tag{6}$$

$$\mathbf{u}^{n+1} = \mathbf{u}^* - \Delta t \mathcal{G}\phi^n. \tag{7}$$

The key elements of the present IBM are the transformations between the Eulerian mesh and the Lagrangian one, which are carried out through the interpolation and spreading operators, $\mathcal{I}$ and $\mathcal{C}$. These two operators are built using a modified Reproducing-Kernel Particle Method (RKPM) [12] that ensures a bijection between the interpolation and spreading operations, implying that the integral of the force is the same when computed in the Lagrangian or Eulerian frames. Important properties of the algorithm are the preservation of the global accuracy of the underlying differencing scheme, and the sharpness with which the interface is resolved. For further details the reader is referred to the work of Pinelli et al. [12].

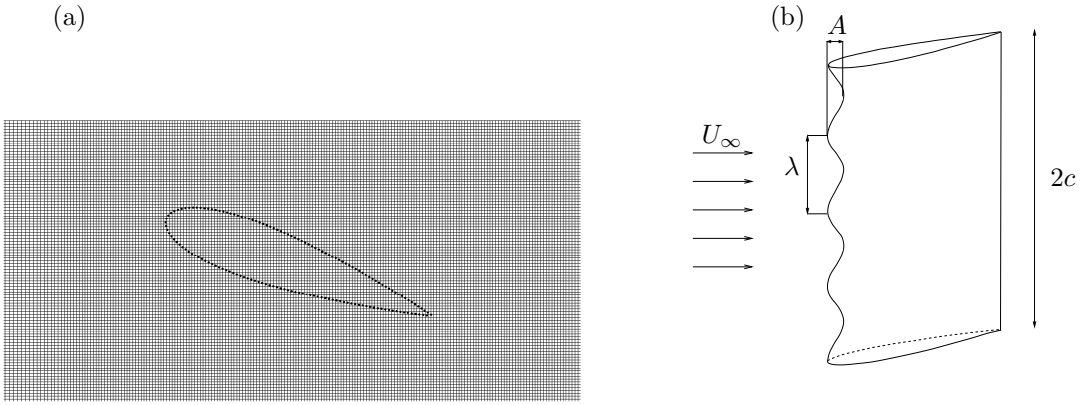

Figure 2. Model of the airfoil geometry. (a) Set of Lagrangian points plotted with the underlying Eulerian fluid mesh. (b) Undulated leading edge, showing the parameters of control λ and A. The span length is equal to $2c$.

2.2. *Numerical setup*

The baseline mesh chosen for all the simulations is cartesian, uniform in the z-direction, and non-uniform in x (streamwise direction) and y (normal to the freestream direction). To ensure a fine clustering of the points near the airfoil, a stretching factor of 1.02 is introduced in both x and y-directions. The mesh is made of 6×10^6 points ($512 \times 386 \times 32$ in x, y and z directions, respectively). The computational box dimensions along the x, y and z coordinates are $38c \times 17c \times 2c$ (c being the average chord length), respectively. The chosen box size is large enough to avoid spurious effects due to the outer boundary conditions. In particular, at the inlet and outlet, the boundary conditions are set to uniform inflow and zero-velocity derivative. The top and bottom boundaries are planes of symmetry, and periodic conditions are used in the the spanwise direction. A spanwise cross section of the mesh in the region occupied by the airfoil is shown in Figure 2(a).

The baseline airfoil geometry has a thickness of 20 % of the chord, and follows the shape of a NACA0020 foil. To model the tubercles, a geometrical waviness on the leading edge is introduced, taking the form of a sinusoidal function along the span: $f(t) = A^* \cos(2\pi z/\lambda^*)$, where $A^* = A/c$ is the non-dimensional amplitude, $\lambda^* = \lambda/c$ is the non-dimensional wavelength (Figure 2(b)). An optimization algorithm is used to distribute evenly the Lagrangian markers so that each Eulerian cell contains one marker (a condition required to obtain a reliable behaviour of the IBM [12]).

A validation study was first performed on a NACA0012 airfoil at a 20^o angle of attack to compare the present results with data obtained at a Reynolds number of $Re = 800$ by Bourguet et al. [10]. Typical values of mean lift and drag coefficients and Strouhal number ($St = fc/U_\infty$, where f is the frequency of vortex shedding) were used to assess the grid convergence of the simulation, and were found to be in good agreement with the mentioned study when using the mesh described above.

3. Results and discussion

To assess the hydrodynamic performance of the airfoil, the drag and lift coefficients defined by:

$$C_d = \frac{F_d}{(\rho U_\infty^2/2) s\, c} \quad ; \quad C_l = \frac{F_l}{(\rho U_\infty^2/2) s\, c}, \tag{8}$$

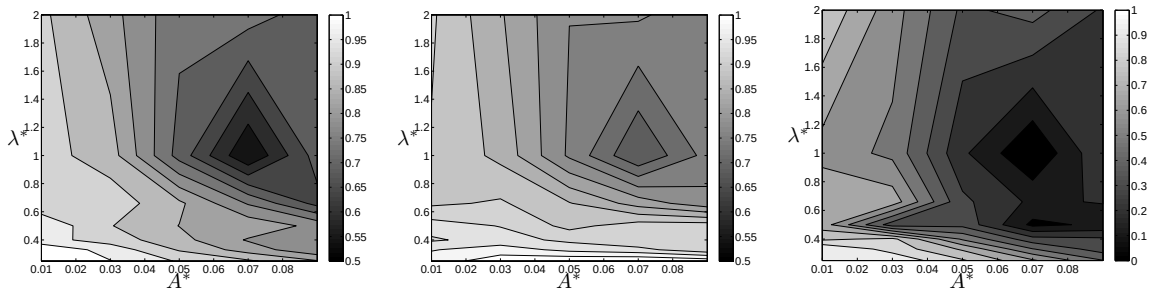

Figure 3. Contours of the performance ratios varying the amplitude A^* and the wavelength λ^*. (a) R_1; (b) R_2; (c) R_3.

were monitored. In (8), ρ is the fluid density, U_∞ is the freestream velocity, s is the wing span, and F_d and F_l are the projections on the x- and y-axis of the aerodynamic force. In addition, three ratios based on these coefficients:

$$R_1 = \frac{< C_d >}{< C_{d,b} >} \quad ; \quad R_2 = \frac{< C_l >}{< C_{l,b} >} \quad ; \quad R_3 = \frac{C_l'}{C_{l,b}'}, \tag{9}$$

are defined. In (9), $< . >$ represents averaging over time (typically performed over 10 vortex shedding cycles), the subscript b refers to the baseline case (the one with a straight leading edge), and the lift fluctuations are defined by $C_l' = \max(C_l - < C_l >)$. Improving the hydrodynamic performances of the airfoil translates into having $R_1 < 1$, $R_2 > 1$ and $R_3 < 1$.

We performed a parametric study varying the amplitude A^* from 0 (straight leading edge) to 0.1, and the wavelength λ^* from 0.25 to 2.0. Note that $A^* = 0.1$ corresponds to an amplitude of the bumps of 10% of the chord, and a wavelength of 2.0 corresponds to two periods of spanwise leading-edge waves per chord distance.

Contour plots of the ratios R_1, R_2 and R_3 defined in (9) are shown in Figure 3 as functions of A^* and λ^*. Values of these ratios close to unity, which are observed for low amplitudes of the bumps and low wavelengths, indicate that there is no effect of the leading-edge waves on the flow in these geometries. The contours of R_1 (Figure 3(a)) show a maximum drag reduction at $\lambda^* \simeq 1$ and $A^* \simeq 0.07$, a case also associated to lift reduction (Figure 3(b)) and also to a drastic reduction of lift fluctuations (Figure 3(c)).

Next, we focus on the flow structure modifications that occur when fixing $\lambda^* = 1$, a value common to all the minima of the ratios (9), as shown in Figure 3, while varying the amplitudes A^*. In Figure 4(a) we observe a decrease in drag (up to 35%), when increasing A^* up to a minimum, which occurs for $A^* = 0.07$. We also note, in Figure 4(b) the same decreasing trend of the mean lift coefficient. This may be due to the low value of Re for the present study, which is several orders of magnitude lower than the one considered in the experiments, where turbulent conditions are usually found. At $\lambda^* = 1$ and $A^* = 0.07$ the minima for the drag and lift coefficients are accompained by a complete cancellation of lift fluctuations, indicating the establishment of a quasi-steady wake and a strong weakening of the shedding. An almost-steady behaviour is found, in which the time fluctuations of the baseline Von Kàrmàn instability disappear. The spectrum of the lift coefficient, shown in Figure 5, indicates that as the undulation amplitude increases, the spectrum tends to flatten, and no frequency peak is recorded for the case corresponding to $A^* = 0.07$, which confirms the trend mentioned above.

To gain more insight on the effects of these changes on the topology of the flow, Figure 6 shows isosurfaces of zero longitudinal velocity for the straight leading edge, compared with the case $\lambda^* = 1$ and $A^* = 0.03$. In these plots the zone inside the 3D envelope corresponds to negative longitudinal velocity, *i.e.*, recirculating fluid. It appears that one of the effects of the bumps is to modify the topology of the

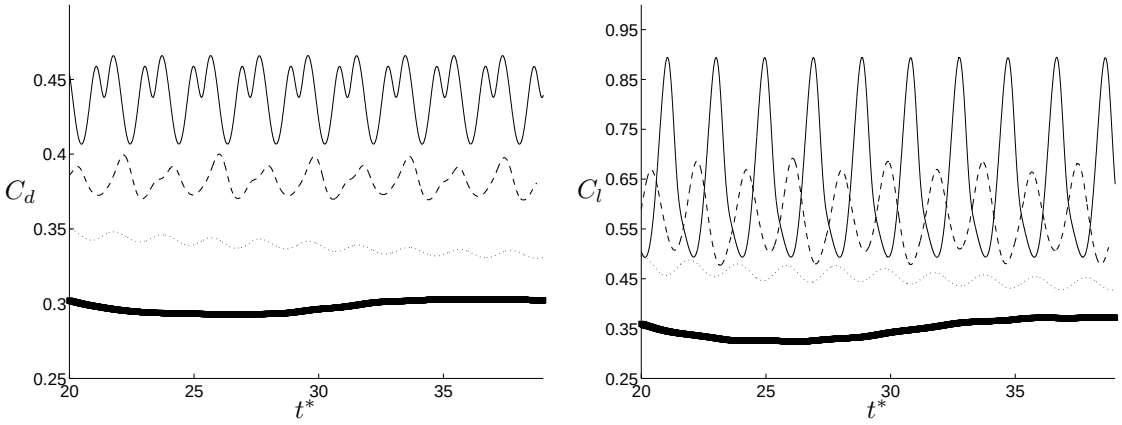

(a) (b)

Figure 4. (a) Drag coefficient and (b) lift coefficient for $\lambda^* = 1$, varying the amplitude of the leading-edge bumps. Plain line: baseline case ($A^* = 0$). Dashed line: $A^* = 0.03$. Dotted line: $A^* = 0.05$. Thick line: $A^* = 0.07$.

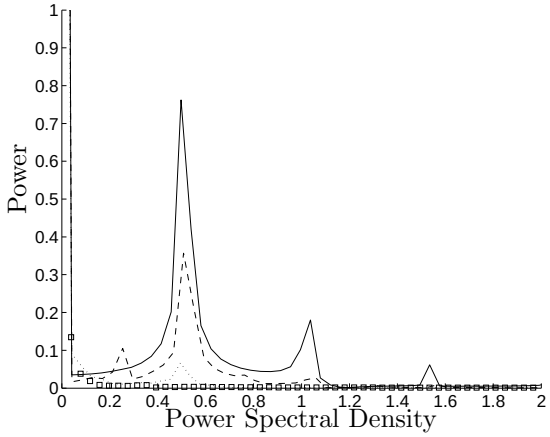

Figure 5. Spectrum of lift coefficient. Plain line: baseline case ($A^* = 0$). Dashed line: $A^* = 0.03$. Dotted line: $A^* = 0.05$. Squares: $A^* = 0.07$.

separation zone along the spanwise direction. In Figure 6(b) this effect takes the form of two localized regions downstream of each bumps. Although the leading-edge bumps affect the shape of the recirculating zone, its global size is nearly the same for both cases.

In Figure 7 the recirculation zone for two other cases, including the one characterized by the minimum force coefficients ($\lambda^* = 1.0$ and $A^* = 0.07$) are shown. The major difference observed between the latter case and all the others is the fact that the boundary layer is partially attached at the spanwise location corresponding to the tip of the bumps (a behaviour that does not occur for other wavelengths). This partial reattachment was also observed by Weber et al. [20]. Conversely, the global size of the recirculating zone is strongly increased, compared to the baseline case. In this particular regime, the wake is completely dominated by the presence of two strong streamwise rolls, as displayed in Figure 8; these rolls do not oscillate, as demonstrated by the corresponding spectrum of Figure 5. Also, as shown in Figure 4, these structures have an "anti-lift" action due to the recirculation zone created by the rolls, which pushes the fluid downwards on the suction side of the airfoil, thus counterbalancing the lift force.

(a) (b)

Figure 6. Recirculating regions shown by isosurfaces of zero longitudinal velocity. (a) Baseline case; (b) $A^* = 0.03$ and $\lambda^* = 1$.

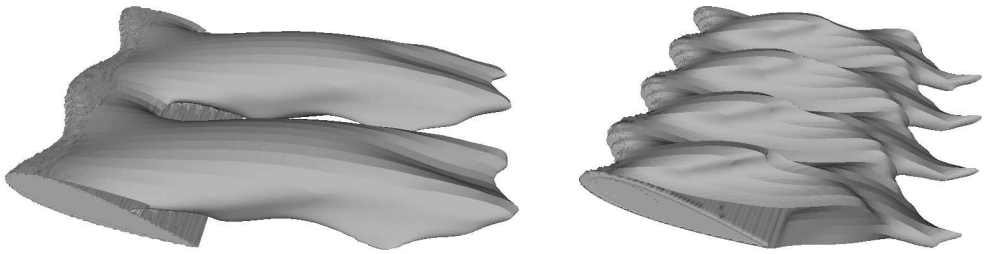

(a) (b)

Figure 7. Recirculation regions shown by isosurfaces of zero longitudinal velocity. (a) $A^* = 0.07$, $\lambda^* = 1$; (b) $A^* = 0.07$, $\lambda^* = 0.5$.

For other wavelengths these effects are still present but with a smaller impact. Figure 7(a) shows that for the same amplitude of the bumps but $\lambda^* = 0.5$ the topology of the flow is quite different and the flow is fully separated along the span. This configuration also exhibits higher lift fluctuations, as shown in Figure 3(c).

For $A^* < 0.07$, the streamwise rolls are still present but their intensity appears to be too weak to stabilize completely the separation region. Let us mention that in experimental studies at higher Reynolds numbers [6,1], PIV measurements show the trace of these streamwise rolls. Fish et al. [19] suggest a similar scenario claiming that the pairs of counter-rotating vortices generated on each side of the bump are generated through a mechanism similar to the one observed on a delta wing.

To shed more light on the flow dynamics, in Figure 8 we show instantaneous flow visualizations of two cases, one ($A^* = 0.07$, $\lambda^* = 1$) in which we observe a significant drag/lift reduction and another ($A^* = 0.03$, $\lambda^* = 1$) in which streamwise rollers are not strong enough to modify the wake. In both cases we show isosurfaces of the second invariant of the gradient of the velocity fluctuation Q' defined by:

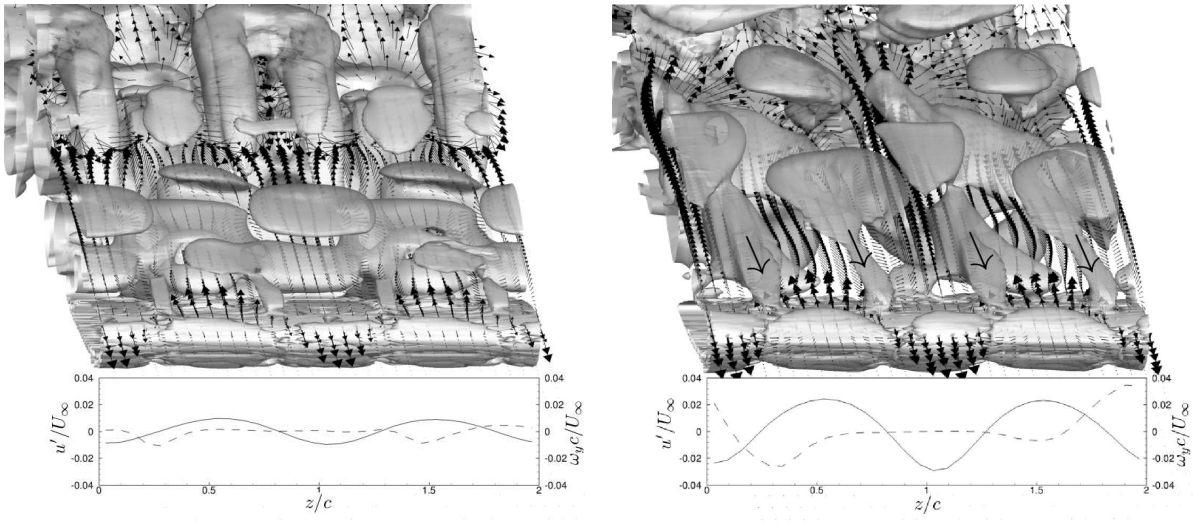

(a) (b)

Figure 8. Isosurfaces of Q' and velocity fluctuation vectors in the plane $y = 0.05c$ (front view), and profiles of u' (solid line) and ω_y (dashed line) along a line parallel to the leading edge. (a) $A^* = 0.07$, $\lambda^* = 1$; (b) $A^* = 0.03$, $\lambda^* = 1$.

$$Q' = -\frac{1}{2}\frac{\partial u_i'}{\partial x_j}\frac{\partial u_j'}{\partial x_i}, \tag{10}$$

where $u_i' = u_i - \langle u_i \rangle_z$, and $\langle \cdot \rangle_z$ represents averaging in the spanwise direction. The second invariant of the velocity gradient tensor has been shown to be effective in visualizing the coherent structures in turbulence [22,21]. In the same figure, we also show the velocity fluctuation vectors in a horizontal plane near the leading edge, and the velocity fluctuations and vertical vorticity along a spanwise line in correspondance with the mean leading edge at an height of $\simeq 0.15\ c$ over the mean wing surface.

As expected, in both cases we observe that the velocity is lower near the crests and higher in the valleys. The fluctuating velocity forms an array of alternating jets pointing forwards and backwards. Correspondingly, regions of alternating shear (reflected by the behaviour of the normal vorticity fluctuactions) are formed, with maximum shear corresponding to inflection points in the velocity-fluctuation profile. Under those circumstances, it is expected that a Kevin–Helmholtz instability should produce rolls of vorticity pointing in the direction normal to the surface in the leading edge region. Those vortical tubes are visible in Figure 8, where they appear in form of vorticity tongues emanating from the near-wall region (in Figure 8(b) we have used arrows to indicate their positions). In particular, the vorticity appears to roll up into a vortex tube which is initially vertical, and then immediately tilted into the streamwise direction, as it is advected by the mean stream. This Kelvin-Helmholtz-driven scenario suggests a completely different mechanism for the generation of the streamwise rollers than the "delta wing" one proposed by other authors [1,19] and is similar to conceptual models for the generation of quasi streamwise vortices from the destabilization of wall streaks in near wall turbulence [23].

Additionally, the action of the streamwise rolls generated explains the local reattachment of the boundary layer over the bumps seen on Figure 7(a), (*i.e.*, in the case of $A^* = 0.07$, $\lambda^* = 1$). As indicated by the vectors of the fluctuating velocity field in Figure 8(b), the flow is accelerated downstream of the bumps, which is not the case in Figure 8(a). This is related to the presence of the counter-rotating streamwise vortices which tend to accelerate the fluid in between them by adding momentum, and thus confer to the fluid the extra amount of kinetic energy necessary to prevent local separation. This analysis, obtained in

a massively separated flow configuration, is in good agreement with the one proposed recently in [19] to explain the delay of stall angle observed in the presence of leading edge bumps.

4. Conclusions

To assess the fundamental effects induced by the geometrical modulation of the leading edge of an infinite wing, a numerical investigation has been performed on a NACA0020 wing profile presenting a wavy leading edge, at low Reynolds number ($Re = 800$), and in a configuration of massively separated boundary layer ($\alpha = 20^o$). The waviness was introduced using a sinusoidal variation along the span of wavelength λ^* and amplitude A^*, and periodic boundary conditions along the same direction were used, for both fluid and wing geometry.

A parametric study on the effect of the wavelength and the amplitude of the leading-edge wave has been carried out. It has been found that a certain choice of the two parameters modify drastically the topology of the wake: $\lambda \simeq 1\ c$, and an amplitude of the bump equals to 7 % of the chord. In this configuration, the shedding regime disappears, the flow is dominated by streamwise structures generated by the bumps and the boundary layer is partially attached to the wall in correspondance with the crests positions.

The influence of these streamwise structures on the boundary layer separation has been studied and a physical mechanism identified to explain the local reattachment observed downstream of the bumps. Moreover, a Kelvin-Helmholtz-like instability driven by the spanwise modulation of the streamwise velocity profile is proposed to be at the origin of the generation of the streamwise vortices which control the boundary layer separation.

In the future, higher Reynolds numbers, close to those observed in nature, and at least large enough to achieve fully turbulent regimes over the airfoil, need to be considered to explain the moderate increase in the lift coefficient observed in the experiments. Further investigations are also required to support the conceptual model proposed in this work to explain the generation of the streamwise rolls, and their subsequent effects on the boundary layer separation. Finally, it could be of interest to study the effects on heterogeneous bumps over the span, with different amplitudes along the span and decreasing wavelength near the tip of the wing, as illustrated on Figure 1.

References

[1] M. J. Stanway, Hydrodynamic effects of leading-edge tubercles on control surfaces and in flapping foil propulsion, Master of Science thesis, MIT, 2008.

[2] D. M. Bushnell, K. J. Moore, Drag Reduction in Nature, Annu. Rev. Fluid Mech., 23 (1991) 65–79.

[3] F. M. Fish, J. M. Battle, Hydrodynamic design of the humpback whale flipper, J. Morphology, 225 (1995) 51–60.

[4] P. Watts and F. E. Fish, The influence of passive, leading edge tubercles on wing performance. In Proc. 12th UUST, Durham, New Hampshire, August 2001.

[5] D. S. Miklosovic, M. M. Murray, L. E. Howle, F. E. Fish Leading-edge tubercles delay stall on humpback whale (Megaptera novaeangliae) flippers, Phys. Fluids, 16 (5) (2004) 39–42.

[6] H. Johari, C. Henoch, D. Cosutodio, A. Levshin, Effects of leading-edge protuberances on airfoil performance, AIAA J., 45 (11) (2007) 2634–2642.

[7] E. G. Paterson, R. V. Wilson, F. Stern, General-purpose parallel unsteady RANS CFD code for ship hydrodynamics, IIHR Hydrosci. Eng. Rep. 531 (2003), Univ. Iowa, Iowa.

[8] E. A. van Nierop, S. Alben, M .P. Brenner, How bumps on whale flippers delay stall: An Aerodynamic Model, Phys. Rev. Lett., 100 (2008) 054502.

[9] F. E. Fish, G. V. Lauder, Passive and active flow Control by swimming fishes and mammals, Annu. Rev. Fluid Mech., 38 (2006) 193–224.

[10] R. Bourguet, M. Braza, A. Sevrain, A. Bouhadji, Capturing transition features around a wing by reduced-order modeling based on compressible Navier-Stokes equations, Phys. Fluids, 21 094104 (2009).

[11] C. S. Peskin, Flow patterns around heart valves: a numerical method, J. Comput. Phys. 10 (1972) 252–271.
[12] A. Pinelli, I. Z. Naqavi, U. Piomelli, J. Favier, Immersed-boundary methods for general finite-difference and finite-volume Navier-Stokes solvers, J. Comput. Phys. 229 (2010) 9073–9091.
[13] F. H Harlow, E. Welch, Numerical calculation of time-dependent viscous incompressible flow of fluid with free surface, Phys. Fluids, 8 (12) (1965).
[14] A. J. Chorin, Numerical solution of Navier-Stokes equations, Math. Comput. 22 (104) (1968) 745–762.
[15] J. Kim, P. Moin, Application of a fractional step method to incompressible Navier-Stokes equations, J. Comput. Phys. 59 (1985) 308–323.
[16] J. Van Kan, A second-order accurate pressure-correction scheme for viscous incompressible flow, SIAM J. Sci. Stat. Comput. 7 (1986) 870–891.
[17] M. Uhlmann, An immersed boundary method with direct forcing for the simulation of particulate flows, J. Comput. Phys. 209 (2) (2005) 448–476.
[18] C. H. K. Williamson, Defining a universal and continuous Strouhal–Reynolds number relationship for the laminar vortex shedding of a circular cylinder, Phys. Fluids, 31 2742 (1988).
[19] F. E. Fish, P. W. Weber, M. M. Murray, L. E. Howle, The humpback whales flipper: Application of bio-inspired tubercle technology, Integrative and Comparative Biology (2011).
[20] P. W. Weber, L. E. Howle, M. M. Murray, D. S. Miklosovic, Computational evaluation of the performance of lifting surfaces with leading edge protuberances, J. Aircraft 48 (2011) 591–600.
[21] Y. Dubief, F. Delcayre, On coherent-vortex identification in turbulence, J. of Turbulence 1 (2000) 1–22.
[22] J. C. R. Hunt, A. A. Wray, P. Moin, Eddies, streams, and convergence zones in turbulent flows, studying turbulence using numerical simulation databases, 2. Proceedings of the 1988 Summer Program. Stanford University (1988) 193–208.
[23] G. Kawahara, J. Jimenez, M. Uhlmann, A. Pinelli, Linear instability of a corrugated vortex sheet – a model for streak instability, J. Fluid Mech. 483 (2003) 315–342.